

Experimental performance of Y-shaped eccentrically braced frames fabricated with high strength steel

Ming Lian^{1,2a}, Mingzhou Su^{*1} and Yan Guo^{1b}

¹ School of Civil Engineering, Xi'an University of Architecture and Technology, Xi'an 710055, P.R. China

² Post-doctoral Mobile Stations of Material Science and Engineering, Xi'an University of Architecture and Technology, Xi'an 710055, P.R. China

(Received November 03, 2016, Revised March 29, 2017, Accepted May 05, 2017)

Abstract. In Y-shaped eccentrically braced frame fabricated with high strength steel (Y-HSS-EBF), link uses conventional steel while other structural members use high strength steel. Cyclic test for a 1:2 length scaled one-bay and one-story Y-HSS-EBF specimen and shake table test for a 1:2 length scaled three-story Y-HSS-EBF specimen were carried out to research the seismic performance of Y-HSS-EBF. These include the failure mode, load-bearing capacity, ductility, energy dissipation capacity, dynamic properties, acceleration responses, displacement responses, and dynamic strain responses. The test results indicated that the one-bay and one-story Y-HSS-EBF specimen had good load-bearing capacity and ductility capacity. The three-story specimen cumulative structural damage and deformation increased, while its stiffness decreased. There was no plastic deformation observed in the braces, beams, or columns in the three-story Y-HSS-EBF specimen, and there was no danger of collapse during the seismic loads. The designed shear link dissipated the energy via shear deformation during the seismic loads. When the specimen was fractured, the maximum link plastic rotation angle was higher than 0.08 rad for the shear link in AISC341-10. The Y-HSS-EBF is a safe dual system with reliable hysteretic behaviors and seismic performance.

Keywords: dynamic properties; eccentrically braced frames (EBFs); high strength steel (HSS); seismic performance; experimental study

1. Introduction

Eccentrically braced frames (EBFs) have evolved from two existing lateral force resistant systems; moment-resisting frames (MRFs) and concentrically braced frames (CBFs). MRFs offer properties of ductility and energy dissipation at the expense of its low stiffness. CBFs have high stiffness, but smaller energy dissipation capabilities. EBFs were developed to incorporate the best offered by the MRFs and CBFs. Earthquake energy can be dissipated through plastic deformation of the links in EBFs. EBFs are reliable structural systems exhibiting satisfactory seismic performance (Bosco and Rossi 2009, Lin *et al.* 2010, Dusicka *et al.* 2010, Shayanfar *et al.* 2012, Ioan *et al.* 2013, 2016, Mansour *et al.* 2014, Speicher and Harris III 2016, Wang *et al.* 2016). As a result, the improvements in the mechanical properties and weldability of high strength steels, along with the availability of improved welding consumables and welding processes, have allowed high strength steel to become an economical alternative for conventional steel. At a time when high strength steel was widely used in bridge structures (Shim *et al.* 2011, Chen *et al.* 2012, Barbosa *et al.* 2016), it began to appear in building structure designs (Tokgoz *et al.* 2012, Wang *et al.* 2014, Ma *et al.* 2016).

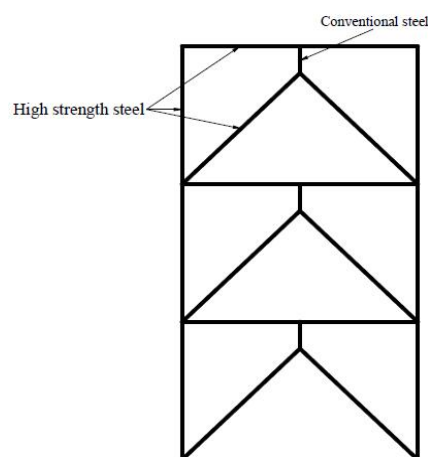


Fig. 1 HSS-EBFs

In eccentrically braced frames fabricated with high strength steel (HSS-EBFs), links are made of conventional steel; other structural members are made of high strength steel, which is shown in Fig. 1. As a point of reference, “conventional steel” is defined as the steel with a specified nominal yield stress up to 345 MPa, whereas “high strength steel” is defined as the steel with a specified nominal yield stress above 345 MPa. Column, beam, and brace members of the HSS-EBF are designed to remain in the elastic stage or have slight plastification while links enter the plastic stage completely during rare earthquakes (2% probability of exceedance in a 50-year period). This structure can satisfy the seismic design requirements with no demands of plastic

*Corresponding author, Ph.D., Professor,
E-mail: sumingzhou@163.com

^a Ph.D., E-mail: lianming0821@163.com

^b Professor, E-mail: gy623812@126.com

Table 2 Mechanical properties of steel in the test specimen

Steel	Thickness	Yield strength	Ultimate strength	Elastic modulus	Elongation ratio
	t (mm)	f_y (MPa)	f_u (MPa)	E ($\times 10^5$ MPa)	(%)
Q345	6	427.40	571.10	2.01	26.53
Q345	10	383.33	554.40	2.00	31.01
Q460	6	496.90	658.57	2.08	29.73
Q460	10	468.77	627.97	2.02	35.88

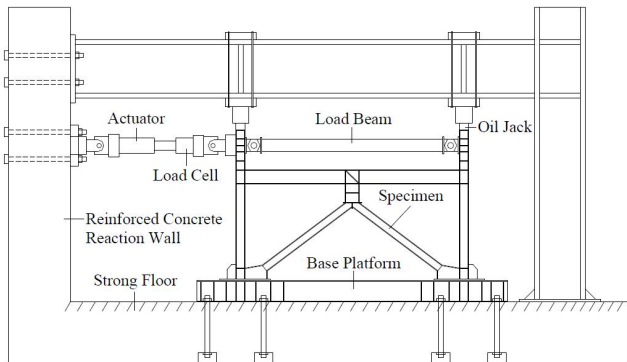


Fig. 4 Test setup

axial compression deformation occurred at the beam, which would affect the performance of the specimen. Thus, using load beam could avoid the axial compression deformation occurring at the beam. In order to consider the influence of the vertical load transferred from the upper layers and P-delta effects to the behavior of the specimen, a constant axial load of 400 kN was applied based on the vertical load in the prototype structure, and using an oil jack pushing against the top of the column. The cyclic loading condition was generated using an actuator that was connected to the specimen. The loading history is shown in Fig. 4. As seen from Fig. 5, the test loads began with a load control stage in which the cyclic load reversals were applied until obvious stiffness degradation could be observed in the hysteretic curves of the specimen, and the corresponding displacement was defined as the yield displacement (Δ_y). The following was displacement controlled. In this stage, the specimen was tested under displacement control for three cycles with the magnitude of $\pm \Delta_y, \pm 2\Delta_y, \pm 3\Delta_y, \pm 4\Delta_y, \pm 5\Delta_y, \dots$ Fig. 6 shows the distribution of the strain gauges and rosettes on the specimen.

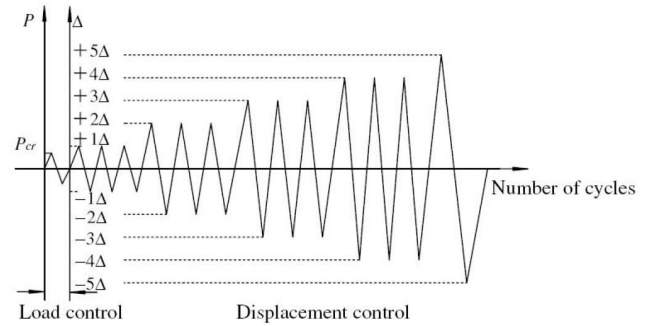


Fig. 5 Loading history

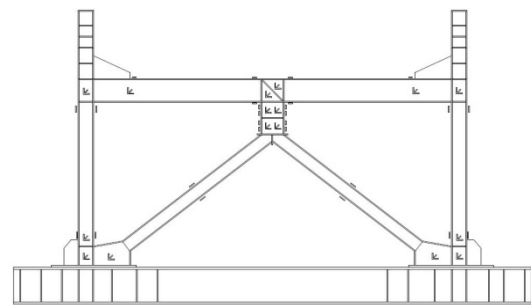


Fig. 6 Distribution of strain gauges and rosettes

2.3 Test results and discussion

2.3.1 Test phenomena

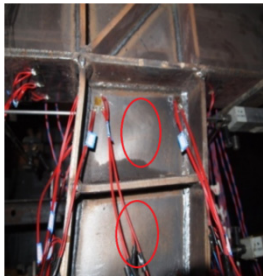
During the test, the link entered the plastic stage firstly. The main deformation occurred at the link, beam-end and column base, respectively. The test was stopped till the link could not resist the loads. Table 3 lists the test phenomena observed at different loading levels, P is the force provided by the actuator, which equals to the base shear force of the specimen, Δ is the horizontal displacement of the specimen.

2.3.2 Hysteretic curve

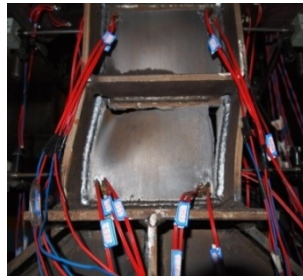
The hysteretic curve is shown in Fig. 8. The curve shows that the specimen had good plastic deformation capacity. The hysteretic curve covered a small area during the load control stage, which shows the elastic behaviors of the specimen. Furthermore, the hysteretic loops were large and did not have obvious degradation in the stiffness and load-carrying capacity within the three cycles of the same displacement level, which indicated that the specimen had a significant energy dissipation capacity. Fig. 9 shows the skeleton curve of the cyclic responses. The curve shows that the base shear force increased before the specimen fractured, which indicated that the specimen had good load-bearing capacity.

2.3.3 Link rotation capacity

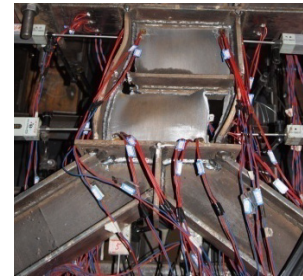
The shear link rotation and plastic rotation angle are shown in Figs. 10 and 11, respectively. The link rotation angle increased with increasing the story drift. The maximum link rotation angle was approximately 30 times higher than the minimum value. When the specimen fractured, the maximum link plastic rotation angle reached



(a) Buckling occurred at link web



(b) link web tore



(c) link web tore



(d) Buckling occurred at column base



(e) Buckling occurred at beam end



(f) Link failure

Fig. 7 Phenomena of the cyclic test

Table 3 Phenomena of the cyclic test

Force provided by actuator (kN)	Horizontal displacement of specimen (mm)	Description of test phenomena	Loading level
+291.9	+3.9	No obvious phenomenon in the elastic region	Load control stage
-408.0	-9.3	The web and flange of the link yield	Δ_y (the 2nd cycle)
-524.4	-18.1	The link and column inclined	$2\Delta_y$ (the 3rd cycle)
+627.1	+27.1	Local buckling occurred at the web of link, as shown in Fig. 7(a)	$3\Delta_y$ (the 3rd cycle)
+630.0	+35.9	The web of the link tore, as shown in Figs. 7(b) and (c)	$4\Delta_y$ (the 1st cycle)
-418.1	-45.0	The weld tore at the end of the link flange	$5\Delta_y$ (the 1st cycle)
+328.0	+43.0	Local buckling occurred at the flange of the column base and web of the beam end, as shown in Figs. 7(d) and (e)	$5\Delta_y$ (the 3rd cycle)
+344.3	+54.0	The link could not continue to resist loads, as shown in Fig. 7(f)	$6\Delta_y$ (the 1st cycle)

*Note: “+” and “-” are the push and pull direction of the actuator, respectively

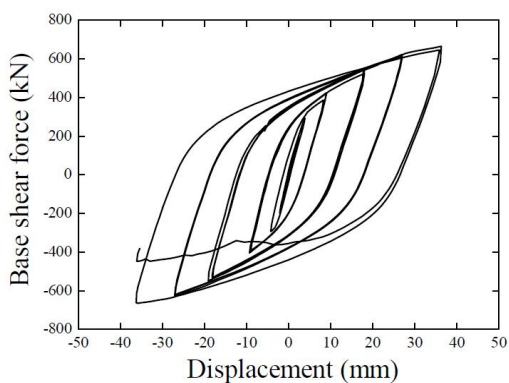


Fig. 8 Hysteretic curve of the test specimen

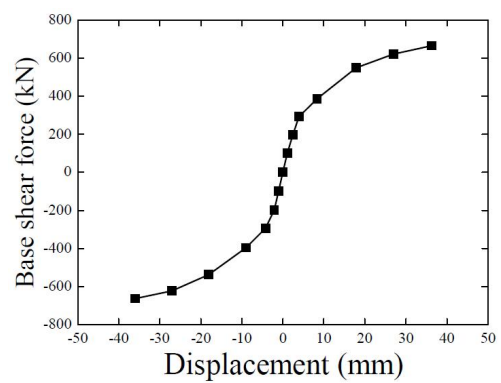


Fig. 9 Skeleton curve

0.10 rad, which was 25% higher than the 0.08 rad of the shear link in AISC341-10 (2010).

2.3.4 Load-bearing, ductility capacity and energy dissipation capacity

The hysteretic behaviors of the specimen can be

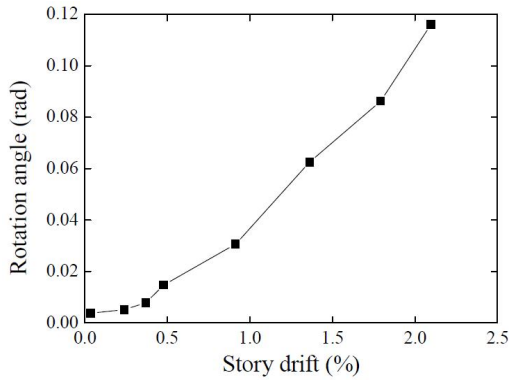


Fig. 10 Link rotation angle

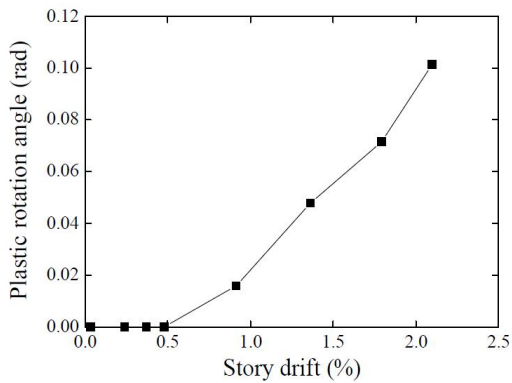


Fig. 11 Link plastic rotation angle

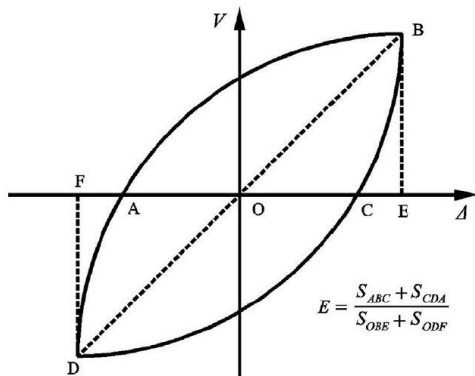


Fig. 12 Calculation of energy dissipation coefficient

Table 4 Load-bearing and ductility capacity

Load direction	Yielding load and displacement		Ultimate load and displacement		Ductility coefficient	
	V_u (kN)	Δ_u (mm)	V_u (kN)	Δ_u (mm)	V_u/V_y	μ
Positive	401.64	8.51	664.86	36.34	1.66	4.27
Negative	377.16	8.16	664.82	36.20	1.76	4.44

* Note: “positive” and “negative” are the push and pull direction of the actuator, respectively

Table 5 Energy dissipation capacity

Loading stage	Story drift (%)	Energy (kJ)	h_e
Load control	100 kN	0.06	—
	200 kN	0.12	—
	300 kN	0.84	0.12
Displacement control	Δ_y	5.14	0.22
	$2\Delta_y$	16.81	0.27
	$3\Delta_y$	31.86	0.30
	$4\Delta_y$	50.37	0.33

evaluated using the load-bearing, ductility, and energy dissipation capability. In this study, ductility coefficient (μ) was used to judge the ductility of the specimen. It is defined as $\mu = \Delta_{max}/\Delta_y$, where Δ_{max} is the maximum displacements. Moreover, the h_e coefficient could be judged depending on the area of the hysteretic loops. It is calculated as $h_e = (S_{ABC} + S_{CDA}) / (S_{OBE} + S_{ODF})$, the S_{ABC} , S_{CDA} , S_{OBE} , and S_{ODF} are shown in Fig. 12.

The yielding load and displacement, ultimate load and displacement, and μ are listed in Table 4. The ratios of the maximum load and yielding load of the specimen were 1.66 at positive direction and 1.76 at negative direction, which indicated that the specimen had good load-bearing capacity after entering the plastic stage. The ratios of the maximum displacement and yielding displacement of the specimen were 4.27 at positive direction and 4.44 at negative direction, which showed that the specimen had good ductility capacity. The energy dissipation capacity of the specimen is shown in Table 5. The dissipated energy

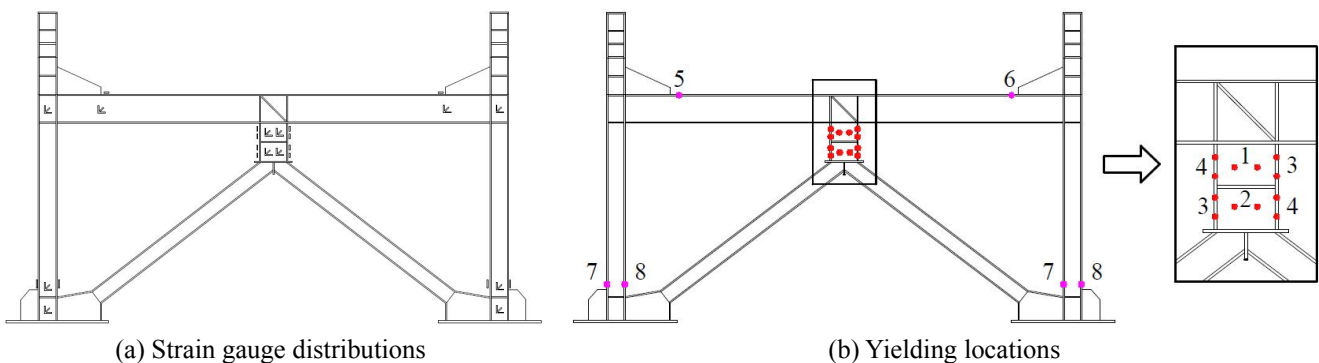


Fig. 13 Strain gauge distributions and yielding locations

and he were increased during the test and the maximum he was 2.75 times higher than the smaller one, which indicated that the specimen had a steady and increasing energy dissipated capacity with the increment of plastic development in the specimen.

2.3.5 Failure mechanism

The yielding locations of the components in the specimen are indicated by circle points in Fig. 13, in which the numbers show the sequence of the structural member yielding. In the load control stage, the specimen remained in the elastic stage. In the Δ_y (1st cycle) displacement level, the yielding was observed at the web in the top grid of the link at location 1. In the Δ_y (2nd cycle) displacement level, the yielding was observed at the web in the bottom grid of the link at location 2. In the Δ_y (3rd cycle) displacement level, the yielding was observed at the link flange at locations 3 and 4. In the $4\Delta_y$ (1st cycle) displacement level, the yielding was observed at the beam flange at locations 5 and 6. Lastly, the yielding in the $4\Delta_y$ (2nd cycle) displacement level was observed at the column flange at locations 7 and 8. Furthermore, the strain values at the link web were higher than those at the link flange, which indicated that the link dissipated the energy via shear deformation.

According to the distribution of the yielding locations, the plastic hinges locate the position of the link, beam end and, column base in the Y-HSS-EBF structure. The distribution of the plastic hinges of the Y-HSS-EBF structure at the ultimate state is shown in Fig. 14.

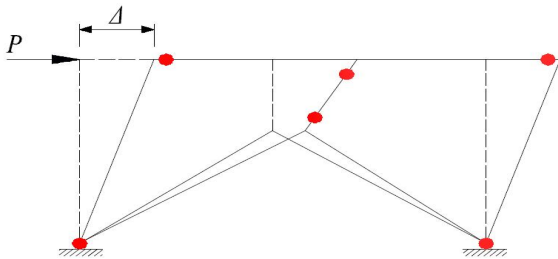


Fig. 14 Distribution of plastic hinges

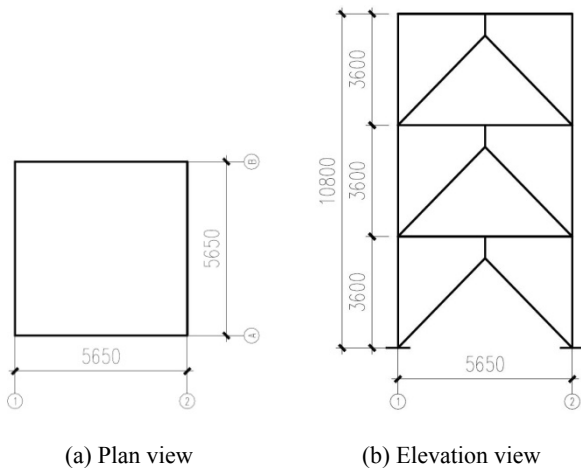


Fig. 15 Dimensions of prototype structure (in mm)

3. Shaking table test

3.1 Test specimen design

A one-bay three-story Y-HSS-EBF was considered as a prototype structure for this study, which is shown in Fig. 15. The prototype was designed by the codes of GB50011-2010 (2010) and JGJ99-98 (1998). The prototype structure was characterized using the peak ground acceleration for an exceeding probability of 10%, equal to 0.2 g, with a 50% exceedance probability in 50 years and moderately firm ground conditions. The factor that reduced the elastic response spectrum to obtain the design spectrum was 4.9 (Su and Li 2014). A damping ratio (ζ) of 5% was used for the design.

Considering the shake table size of 4 m × 4 m and the maximum vertical load carrying capacity of 300 kN, limited the maximum strength capacity of the test specimen (i.e., the maximum base shear and overturning moment). The span of the test specimen was designed to be 2.825 m to fully use the shake table. Thus, the scaling factor of length was calculated as

$$S_l = \frac{2.825}{5.650} = 0.5 \tag{1}$$

The material of the test specimen was identical to that of the prototype structure, which indicates that the scaling factor of the elastic modulus $S_E = 1$. In order to make the total weight of the test specimen smaller than the maximum vertical load carrying capacity of the shake table and did not reduce the horizontal earthquake forces, the similarity ratio of acceleration was taken as $S_a = 1.2$ (the factor did not control the gravity acceleration). Table 6 shows the similarity relationships that were derived according to the dimensions of the parameters (Li 2004) and the “mass-based” similitude law. Moreover, $S_l = 0.5$ and $S_a = 1.2$ were considered according to the properties of the shake table, the mass similarity ratio S_m and others could be calculated

Table 6 Similarity relationships and ratios of the test specimen

Physical quantities	Dimensions	Similarity relation	Ratio of similarity
Strain	—	$S_e = 1$	1
Elastic modulus	FL^{-2}	$S_E = 1$	1
Stress	FL^{-2}	$S_\sigma = S_E S_e$	1
Length	L	$S_l = 0.5$	0.5
Force	F	$S_F = S_\sigma S_l^2 = S_E S_e S_l^2$	0.25
Mass	FT^2L^{-1}	$S_m = S_F / S_a = (S_E S_e S_l^2) / S_a$	0.2083
Density	FT^2L^{-4}	$S_\rho = S_m / S_l^3 = (S_E S_e) / (S_a S_l)$	1.6667
Time/natural period	T	$S_t = S_T = (S_l / S_a)^{-1/2}$	0.6455
Frequency	T^{-1}	$S_f = 1/S_T = (S_l / S_a)^{1/2}$	1.5492
Displacement	L	$S_x = S_l$	0.5
acceleration	LT^{-2}	$S_a = 1.2$	1.2

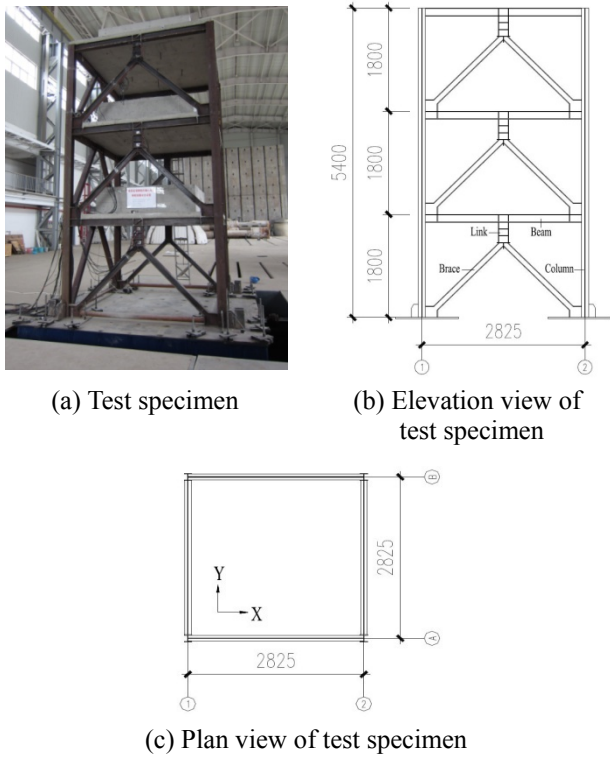


Fig. 16 Dimensions of the test specimen (in mm)

Table 7 Member sections of the specimen

Members	Sections	Material
Beams	H140 × 100 × 8 × 10	Q460
Columns	H145 × 145 × 8 × 10	Q460
Braces	H100 × 100 × 6 × 10	Q345
Links	H180 × 100 × 6 × 10	Q345

*Note: “H” refers to the welded H-shaped section, the following numbers are the section depth (h), flange width (b_f), web thickness (t_w), and flange thickness (t_f), with unit of mm

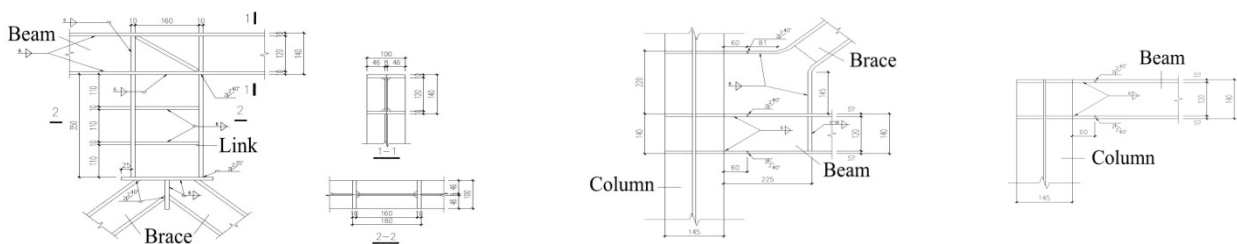


Fig. 17 Details of joints

Table 8 Mechanical properties of steel

Steel	Thickness t (mm)	Yield stress f_y (MPa)	Ultimate strength f_u (MPa)	Elastic modulus E ($\times 10^5$ MPa)	Elongation ratio (%)
Q345	6	414.7	542.03	2.11	28.29
Q345	10	363.8	545.8	2.01	28.74
Q460	8	473.5	635.1	2.12	25.36
Q460	10	516.0	691.97	2.06	23.51

based on the S_i , S_a and material properties. The representative value of the gravity load (G), equals to $1D + 0.5L$, was applied in GB50011-2010 (2010), where D and L are the dead and live load, respectively. Thus, the total mass of the test specimen could be obtained by the G value of the prototype structure and the S_m , which considered the dead and live loads.

The test specimen was constructed as a three-story Y-HSS-EBF with shear links, and one bay in both x - and y -directions (refer to Fig. 16). The story height, span in the x -direction, and span in the y -direction were 1.8, 2.825, and 2.825 m, respectively. The thickness of the reinforced concrete floor was 80 mm. The links were made of Q345 steel (specified nominal yield strength 345 MPa), and the other structural members were made of steel Q460 (specified nominal yield strength 460 MPa). The length of the shear links was 350 mm ($eV_p/M_p = 1.06$). Furthermore, welded joints were used to connect the link to the beam and other elements in the test specimen. The structural member sections are listed in Table 7. The mechanical properties of steel used in the test specimen are presented in Table 8. Fig. 17 shows the details of the joint characteristics.

3.2 Mass of the test specimen

The floor dead load, floor live load, roof dead load, and roof snow load are 5.0, 2.0, 5.625, and 0.125 kN/m², respectively. Furthermore, the wall load is 4.38 kN/m. The representative values of the gravity equal to $1D + 0.5L$ in GB50011-2010 (2010), respectively. According to the dead, live load and the similarity ratio S_m , the total mass of the test specimen was 23.8 t.

3.3 Instrument arrangement

The objectives of this experiment were to obtain the dynamic strain response, acceleration response, and displacement response of the floors. As shown in Fig. 18, there were 19 accelerometers (A1–A19, four on the base

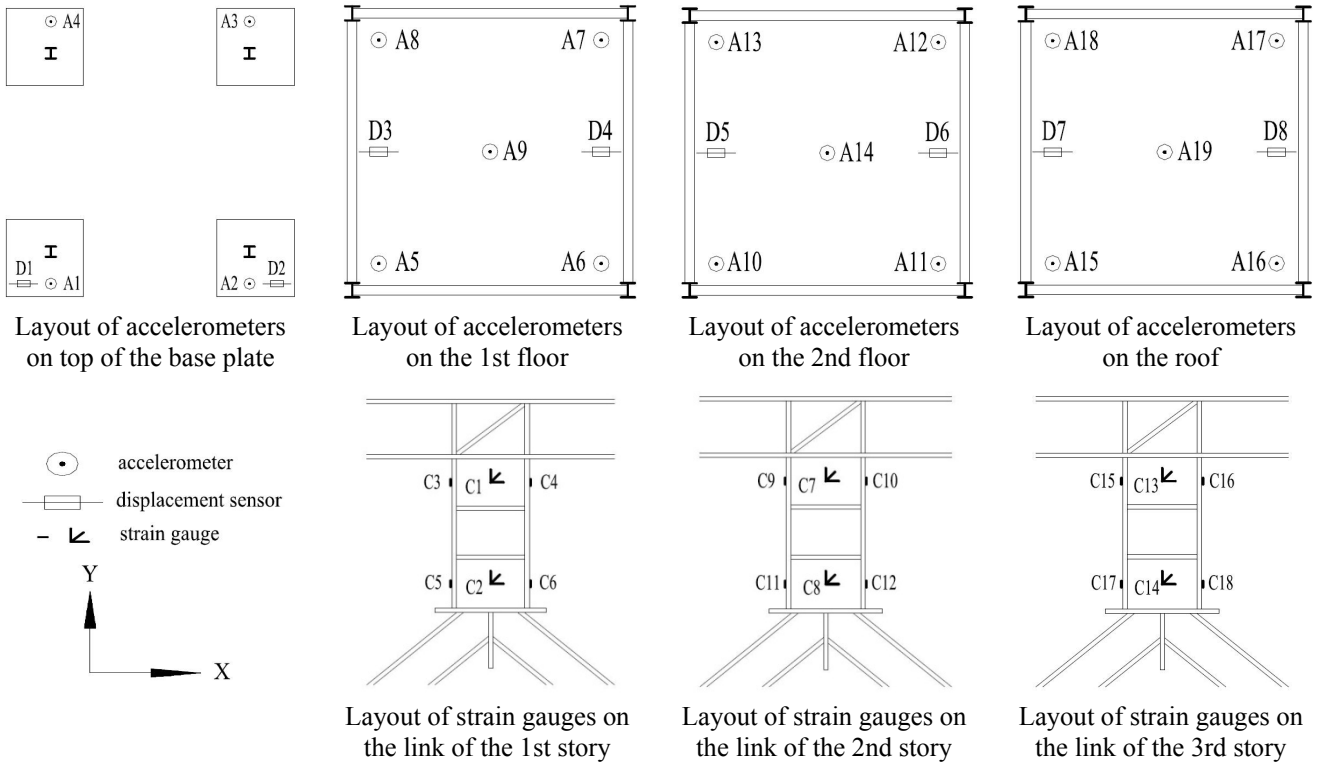


Fig. 18 Layout of monitoring points

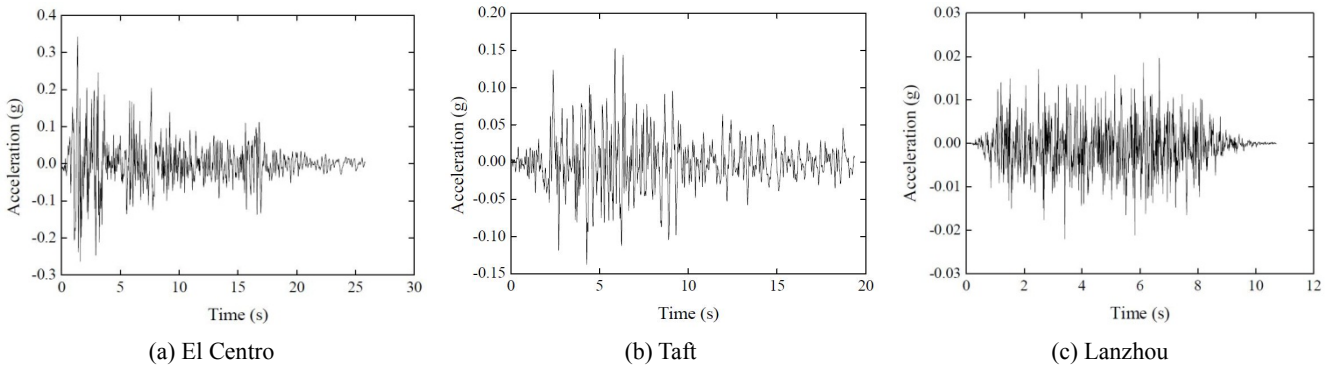


Fig. 19 Acceleration time histories of input ground motions

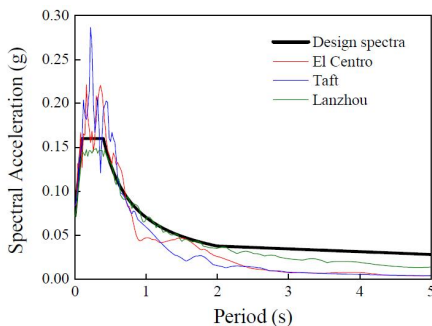


Fig. 20 Spectra comparison of earthquakes with 50% probability of exceedance in 50 years

place and five on each floor) to obtain the acceleration responses, 18 strain gauges on the link of each story (C1–C18) to obtain the strain responses of the links, and eight

displacement sensors (D1–D8, two on the base place and two on each floor) to obtain the displacement responses.

3.4 Loading cases

In order to investigate the effects of different ground motions on the seismic performance of the three-story Y-HSS-EBF specimen, three ground motions were selected as input excitations for the shake table test according to GB50011-2010 (2010), including the El Centro wave (1940), Taft wave (1952), and Lanzhou artificial wave. The time histories of the three ground motions after compress by the time similarity ratio (refer to Table 6) are shown in Fig. 19. Fig. 20 shows the acceleration response spectra of the accelerogram ensemble, along with the design acceleration spectrum. Moreover, the effects of seismic excitation intensity on the seismic performance of the specimen were considered. For each seismic excitation intensity, the

Table 9 List of test cases

Case	Earthquake	Direction	PGA of seismic intensity (g)
1a	WN	X	0.05
1	El Centro		
2	Taft	X	0.042
3	Lanzhou		
2a	WN	X	0.05
4	El Centro		
5	Taft	X	0.084
6	Lanzhou		
3a	WN	X	0.05
7	El Centro		
8	Taft	X	0.12
9	Lanzhou		
4a	WN	X	0.05
10	El Centro		
11	Taft	X	0.168
12	Lanzhou		
5a	WN	X	0.05
13	El Centro		
14	Taft	X	0.24
15	Lanzhou		
6a	WN	X	0.05
16	El Centro		
17	Taft	X	0.264
18	Lanzhou		
7a	WN	X	0.05
19	El Centro		
20	Taft	X	0.48
21	Lanzhou		
8a	WN	X	0.05
22	El Centro		
23	Taft	X	0.744
24	Lanzhou		
9a	WN	X	0.05
25	El Centro		
26	Taft	X	1
27	Lanzhou		
10a	WN	X	0.05

acceleration of the three ground motions were scaled to the corresponding peak ground acceleration (PGA) of the seismic intensity (refer to Table 9). Before each level of PGA, the white noise frequency test was applied to measure the dynamic behavior of the test specimen. Furthermore, the x-direction was the loading direction of all the tests (refer to Fig. 16(c)). Table 8 shows all the loading cases, in which WN stands for the white noise wave. Furthermore, three structural performance levels, i.e., immediate occupancy, life safety, and collapse prevention limit states, were

Table 10 Limit states for shear link (FEMA 356)

Qualitative description	Recommended link rotation (rad)	Corresponding PGAs in Table 4
Immediate occupancy (IO)	0.01	0.084 g
Life safety (LS)	0.115	0.24 g
Collapse prevention (CP)	0.145	0.48 g

Table 11 Test phenomena

Case	PGA (g)	Description of test phenomena
Case 1–3	0.042	No obvious phenomenon in the elastic region
Case 4–6	0.084	No obvious phenomenon in the elastic region
Case 7–9	0.12	No obvious phenomenon in the elastic region
Case 10–12	0.168	No obvious phenomenon in the elastic region
Case 13–15	0.24	The oxide layer peeled off at the weld and the web of the link-beam joint in the first and second story, as shown in Fig. 21(a)
Case 16–18	0.264	The peeling of the oxide layer was slightly observed at the link web and the weld near the flange in the first story, as shown in Fig. 21(b)
Case 19–21	0.48	The oxide layer peeled off at the weld and the link-braces joint in the first and second story, as shown in Fig. 21 (c) The residual link deformation appeared, as shown in Fig. 21 (d)
Case 22–24	0.744	The peeling of the oxide layer was more obvious at the link web and the link-braces joint
Case 25–27	1.0	The residual link deformation was more obvious.

considered for the system assessment carried out in the present study. These limit states for shear links comply with seismic suggestions by FEMA 356. The relationships between seismic performance and the loading cases (refer to Table 4) are summarized in Table 5. Additionally, the prototype structure of the specimen was designed for a PGA of 0.2 g with a 10% exceedance probability in 50 years, while the similarity ratio of acceleration was defined as $S_a = 1.2$ for the shake table test. Thus, the corresponding PGA for the “life safety” level was 0.24 g, as shown in Table 10.

3.5 Test results and discussion

3.5.1 Test phenomena

During each level of the seismic loads, the test specimen’s cumulative structural damage and deformation increased, while its stiffness decreased. When the PGA reached 0.48 g, the residual link deformation appeared. When the PGA reached 1.0 g, no plastic deformation was observed in the braces, beams, or columns, and there was no danger of the test specimen collapse. Table 11 lists the test phenomena observed at different PGA levels.

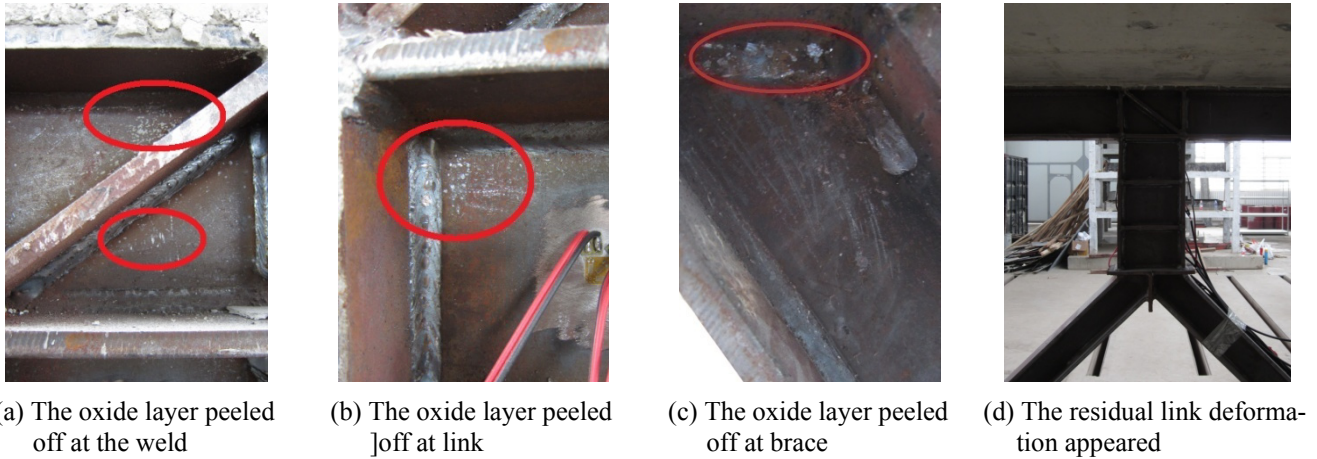


Fig. 21 Observation of the phenomena

Table 12 Scanning frequency and damping ratios of the test specimen

Serial number of the white noise wave	Natural frequency (Hz)	Damping ratio (%)
1a	6.557	3.21
2a	6.550	3.27
3a	6.547	3.37
4a	6.525	3.49
5a	6.500	3.59
6a	6.473	3.72
7a	6.462	3.76
8a	6.404	3.95
9a	6.331	4.08
10a	6.237	4.44

3.5.2 Natural vibration properties

The WN was used to obtain the dynamic properties of the test specimen in the x-direction. Table 12 shows the natural frequency of the vibration and damping ratio of the specimen. As shown in the table, the initial frequency and damping ratio could reach up to 6.557 Hz and 3.21%, respectively. When the seismic load increased, the natural frequency decreased, while the damping ratio increased,

which indicated that the lateral stiffness of the specimen decreased with the increment of the dynamic load.

3.5.3 Acceleration responses

In order to study the acceleration response of the specimen, the acceleration peak value of the stories were divided by that of the structure base. Definite acceleration amplification factor (λ) is defined as follows

$$\lambda = \frac{a_2}{a_1} \tag{2}$$

where a_1 represents the output acceleration of the base of the specimen, and a_2 represents the output acceleration of each story. Therefore, the acceleration amplification factor for each testing point of the specimen was given. The dynamic enlargement curves of each story for all the seismic loads are shown in Fig. 22.

At the same level seismic load, λ increased along the height of the specimen. With the increment of acceleration, the dynamic enlargement curves of different stories had similar trends. Furthermore, with the increment of the seismic intensity, all the dynamic enlargement coefficients of the stories were slightly decreased. This indicated that the plastic damage accumulation with the increment of the seismic load resulted in lateral stiffness degradation of the specimen.

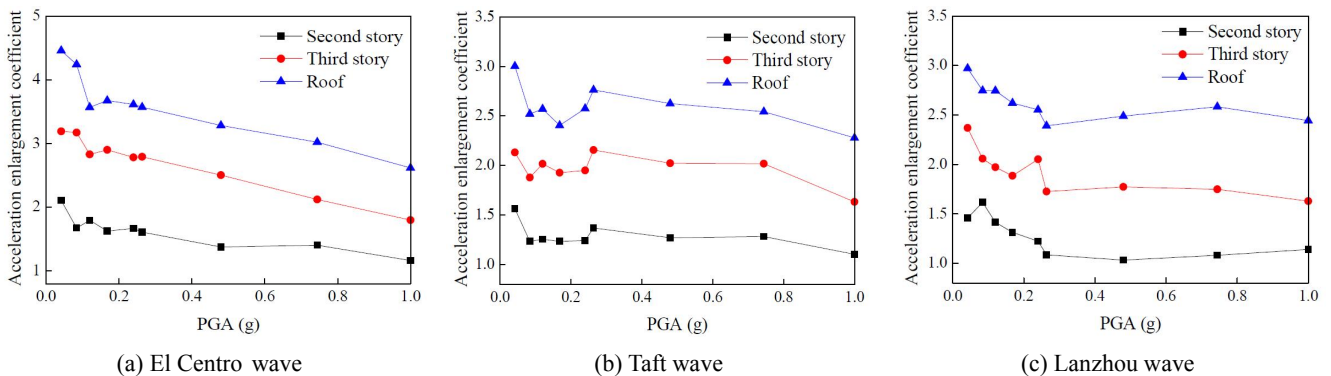


Fig. 22 Acceleration response of the test specimen

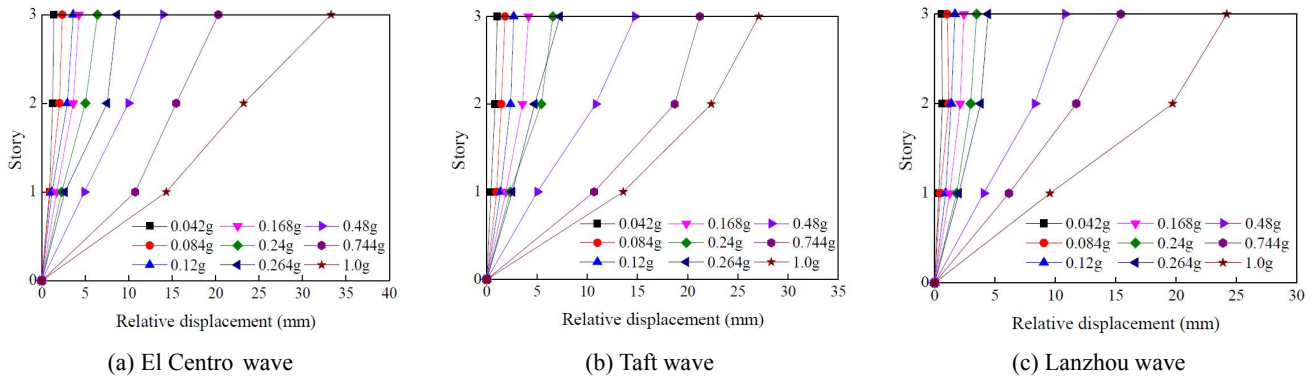


Fig. 23 Maximum relative story displacement for each seismic load

3.5.4 Displacement responses and link rotations

According to the displacement response at the stories and shake table, measured by the displacement sensors, the story displacement was obtained. Fig. 23 shows the maximum relative story displacement of the test specimen in the *x*-direction (refer to Fig. 16(c)). The displacement of each story at the seismic load of the El Centro wave was greater than that of the other seismic loads. In addition, when the acceleration was lower than 0.48 g, there was not much displacement difference in each story, which indicated that the lateral stiffness of the specimen had little degradation. The displacement of the stories obviously increased when the acceleration reached 0.48, 0.744, and 1.0 g, and the displacement increment of the third story was greater than that of the other stories.

Tables 13 and 14 show the maximum interstory drift and link rotations of the test specimen at each seismic load, respectively. The maximum link rotations were 0.005, 0.011

and 0.025 rad when the PGA reached the corresponding values of IO, LS and CP for shear link in Table 10, respectively; these link rotations of test specimen were less than the limitations for the shear link (as seen in Table 10). Furthermore, when the PGA reached 0.24g (corresponding to LS), link rotation was only 0.011 rad, which was lower than the capacity of 0.08 rad for shear link in AISC341-10. It because that the EBF is designed based on the service level earthquake (SLE) with 50% exceedance probability in a 50-year period in GB50011-2010. The demands require that the EBF must remain in elastic stage under the SLE and enter the plastic stage under the maximum considered earthquake (MCE) with 2% exceedance probability in a 50-year period. And the EBF can remain in elastic stage or just slightly enter the plastic stage under the earthquake with 10% exceedance probability in a 50-year period. Moreover, amplify coefficients are used in GB50011-2010 to enlarge the design strength of beam, column and brace to ensure

Table 13 Maximum interstory drifts of the test specimen

PGA (g)	0.042	0.084	0.12	0.168	0.24	0.264	0.48	0.744	1.0
Maximum interstory drift (%)	0.04	0.09	0.14	0.15	0.21	0.33	0.49	0.88	1.37

Table 14 Maximum link rotations of the test specimen

PGA (g)	0.042	0.084	0.12	0.168	0.24	0.264	0.48	0.744	1.0
Maximum rotation (rad)	0.003	0.005	0.008	0.009	0.011	0.016	0.025	0.045	0.070

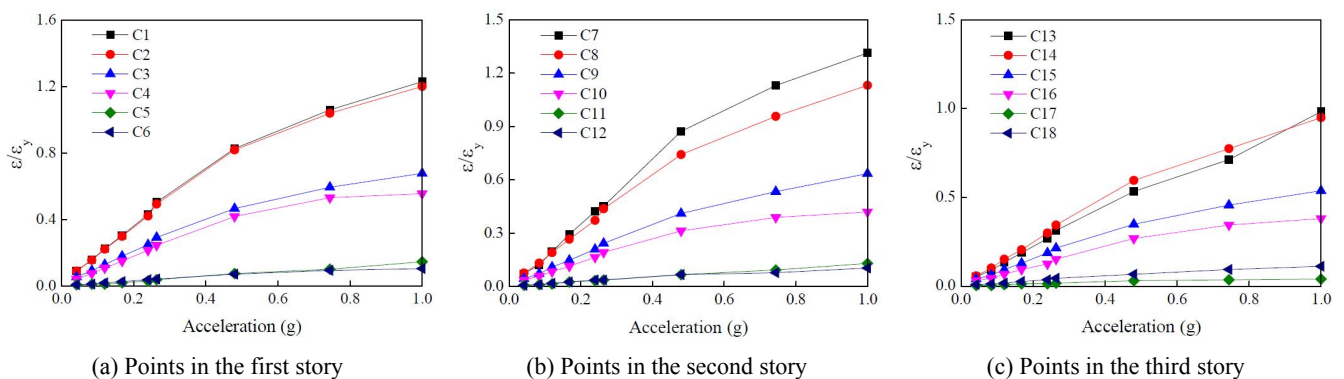


Fig. 24 Variation of strain under the El Centro wave

that the link enter the plastic stage and other structural members remain in elastic stage under the MCE, which results in the oversized cross section of beam, column and brace, and the low link rotation.

3.5.5 Dynamic strain response of links

According to the dynamic strain response of the links by the strain gauges, the values of the dynamic strain increased with the increment of the seismic loads. Furthermore, the dynamic strain response was more obvious when the specimen vibrated during the El Centro wave. Fig. 24 shows the dynamic strain curves of each point at the links during the El Centro wave with different PGA, in which the ratio $\varepsilon/\varepsilon_y$ characterizes the relative strain, where ε and ε_y are the peak strain value and yield strain, respectively. The strain of the webs was higher than that of the flanges, which indicated that the deformation of the links had obvious shearing deformation properties. Moreover, the links dissipated the energy via the deformation of the web.

4. Advantages of HSS-EBFs compared with EBFs

Under the same design conditions, the HSS-EBFs can effectively reduce the overall steel weight because the HSS-EBFs will have smaller member sections relative to EBFs considering the properties of HSS, and HSS-EBFs offer seismic performance equivalent to that of EBFs and improved economy through reduced material costs (Lian and Su 2015). Moreover, because that the ratios of residual stress at critical points in the cross-section to the yield stress are less for HSS columns than for conventional steel columns, and the ratio of residual stress to the yield stress, rather than the magnitude of residual stress itself, which governs the reduction in strength, thus the strength of columns fabricated from HSS have higher strength than that of the columns of equal length and cross-section fabricated from conventional steel when compared on a nondimensional basis (Rasmussen and Hancock 1992, 1995). The ratio is lower for HSS because the magnitude of residual stress is largely independent of the yield stress. It can use a higher value of the slenderness reduction factor for columns used HSS than the value adopted for columns used from ordinary steel (Ban *et al.* 2011), so that the influence of residual stress on the strength of high strength steel columns is reduced in design. It indicated that the stress range is higher and where the strain range is the governing load, HSS has an advantage over conventional steel for low-cycle fatigue (Vander *et al.* 1990). Using HSS for columns and beams can reduce the member sections and structure weight, which can reduce the damage of the earthquakes to structures (Pocock 2006). Additionally, as compared with the EBFs, HSS-EBFs can provide more net areas in the building because of the smaller section of structure members.

5. Conclusions

Cyclic test was used to study the hysteretic behaviors and performance of the Y-HSS-EBF specimen with one-bay and one-story, including the failure mode, load-bearing

capacity, ductility capacity, and energy dissipation capacity. In addition, the shake table test was used to study the dynamic responses of the three-story Y-HSS-EBF specimen, including the dynamic properties, acceleration responses, displacement responses, and strain responses of links. Based on the test reported in this paper, the following conclusions can be drawn within the limitation of the research:

- (1) In the Y-HSS-EBF, when the link was made of Q345 steel with nominal yield strength of 345 MPa entered a plastic stage, the other structural members were made of Q460 steel with nominal yield strength of 460 MPa remained in an elastic stage. Hence, the Y-HSS-EBF is a reliable dual system.
- (2) The hysteretic curves showed the good plastic deformation capacity of the Y-HSS-EBF. The Y-HSS-EBF possessed stable and expanding hysteretic loops with no deterioration in the stiffness and load-bearing capacity. The hysteretic loops were very plump, and it could be inferred that the Y-HSS-EBF had a significant energy dissipation capacity.
- (3) According to the distribution of the yielding locations, the plastic hinges located the positions of the link, beam end, and column base when the Y-HSS-EBF structure reached the ultimate state.
- (4) During the seismic loads, the cumulative structural damage and deformation of Y-HSS-EBF structure increased, while its stiffness decreased. There was no plastic deformation observed in the braces, beams, or columns, and there was no danger of the structure collapse.
- (5) The initial damping ratio of the test specimen was between 3% and 4%, and the damping ratio increased with the plastic damage accumulation. The damping ratio was 38% higher than the initial value when the acceleration reached 1.0 g.
- (6) The story acceleration responses and relative story displacements increased along the height of the structure at the same seismic load. In addition, with the increment of the seismic intensity, there was a slight decrease in all the dynamic enlargement coefficients of the stories.
- (7) The designed shear link dissipated the energy via shear deformation during the seismic loads. The link rotation angle of the Y-HSS-EBF was increased with increasing the story drift. When the structure was fractured, the maximum link plastic rotation angle was higher than 0.08 rad for the shear link in AISC341-10.

References

- AISC 341-10 (2010), Seismic Provisions for Structural Steel Buildings; Chicago, IL, USA.
- Ban, H.Y., Shi, G., Liu, Z., Shi, Y.J., Wang, Y.Q., Xing, H.J. and Li, M.H. (2011), "Experimental study on overall buckling behavior of Q420 high strength equal angle members under axial compression", *J. Build. Struct.*, **32**(2), 60-67.

- Barbosa, A.R., Link, T. and Trejo, D. (2016), "Seismic performance of high-strength steel RC bridge columns", *J. Bridge Eng.*, **21**(2), 04015044.
- Bosco, M. and Rossi, P.P. (2009), "Seismic behaviour of eccentrically braced frames", *Eng. Struct.*, **31**(3), 664-674.
- Chen, A.H., Xu, J.Q., Li, R. and Li, H.L. (2012), "Corrosion resistance of high performance weathering steel for bridge building applications", *J. Iron Steel Res., Int.*, **19**(6), 59-63.
- Dusicka, P., Itani, A. and Buckle, I. (2010), "Cyclic behavior of shear links of various grades of plate steel", *J. Struct. Eng.*, **136**(4), 370-378.
- GB50011-2010 (2010), Code for seismic design of buildings; Beijing, China.
- Ioan, A., Stratan, A. and Dubina, D. (2013), "Numerical simulation of bolted links removal in eccentrically braced frames", *Pollack Periodica*, **8**(1), 15-26.
- Ioan, A., Stratan, A., Dubina, D., Poljansek, M., Molina, M.J., Taucer, F., Pegon, P. and Sabau, G. (2016), "Experimental validation of re-centring capability of eccentrically braced frames with removable links", *Eng. Struct.*, **113**, 335-346.
- JGJ 99-98 (1998), Technical specification for steel structure of tall buildings; Beijing, China.
- Li, Z.X. (2014), Theory and technique of engineering structure experiments; Tianjin, China.
- Lian, M. and Su, M.Z. (2015), "Seismic performance of eccentrically braced frames with high strength steel combination", *Steel Compos. Struct., Int. J.*, **18**(6), 1517-1539.
- Lin, K.C., Lin, C.C.J., Chen, J.Y. and Chang, H.Y. (2010), "Seismic reliability of steel framed buildings", *Struct. Safety*, **32**(3), 174-182.
- Ma, J.L., Chan, T.M. and Young, B. (2016), "Experimental investigation of cold-formed high strength steel tubular beams", *Eng. Struct.*, **126**, 200-209.
- Mansour, N., Christopoulos, C. and Tremblay, R. (2014), "Experimental Validation of Replaceable Shear Links for Eccentrically Braced Steel Frames", *J. Struct. Eng.*, **137**(10), 1141-1152.
- Pocock, G. (2006), "High strength steel use in Australia, Japan and the US", *The Struct. Engr.*, **84**(21), 27-30.
- Rasmussen, K.J.R. and Hancock, G.J. (1992), "Plate slenderness limits for high strength steel sections", *J. Constr. Steel Res.*, **23**(1), 73-96.
- Rasmussen, K.J.R. and Hancock, G.J. (1995), "Tests of high strength steel columns", *J. Constr. Steel Res.*, **34**(1), 27-52.
- Shayanfar, M.A., Barkhordari, M.A. and Rezaeian, A.R. (2012), "Experimental study of cyclic behavior of composite vertical shear link in eccentrically braced frames", *Steel Compos. Struct., Int. J.*, **12**(1), 13-29.
- Shim, C.S., Whang, J.W., Chung, C.H. and Lee, P.G. (2011), "Design of double composite bridges using high-strength steel", *Procedia Eng.*, **14**(12), 1825-1829.
- Speicher, M.S. and Harris III, J.L. (2016), "Collapse prevention seismic performance assessment of new eccentrically braced frames using ASCE 41", *Eng. Struct.*, **117**, 344-357.
- Su, M.Z. and Li, Y.L. (2014), "Study on structural behavior factor of high strength steel composite Y-type eccentrically braced frame based on incremental dynamic analysis", *J. Xi'an Univ. Architect. Technol.*, **46**(5), 635-642.
- Tokgoz, S., Dundar, C. and Tanrikulu, A.K. (2012), "Experimental behaviour of steel fiber high strength reinforced concrete and composite columns", *J. Constr. Steel Res.*, **74**(7), 98-107.
- Vander, V.G.J., De, B.J. and Wardenier, J. (1990), "Low cycle fatigue of tubular T- and X-joints", *Proceedings of the 3rd International Symposium on Tubular Structures*, Lappeenranta, Finland, September, pp. 605-616.
- Wang, B.W., Li, G.Q., Cui, W. and Chen, S.W. (2014), "Seismic behavior of high strength steel welded beam-column members", *J. Constr. Steel Res.*, **102**(11), 245-255.
- Wang, F., Su, M.Z., Hong, M., Guo, Y. and Li, S. (2016), "Cyclic behaviour of y-shaped eccentrically braced frames fabricated with high-strength steel composite", *J. Constr. Steel Res.*, **120**(2), 176-187.

CC